Contrasting trends between peak photosynthesis timing and peak greenness timing across seven typical biomes in Northern Hemisphere mid-latitudes

Zhongxi Ge [a,b], Jing Huang [a,b], Xufeng Wang [c,*], Xuguang Tang [a,b], Lei Fan [a,b], Yinjun Zhao [d,e], Mingguo Ma [a,b,*]

[a] *Chongqing Jinfo Mountain National Observation and Research Station for Karst Ecosystem, School of Geographical Sciences, Southwest University, Chongqing 400715, China*
[b] *Chongqing Engineering Research Center for Remote Sensing Big Data Application, School of Geographical Sciences, Southwest University, Chongqing 400715, China*
[c] *Key Laboratory of Remote Sensing of Gansu Province, Heihe Remote Sensing Experimental Research Station, Cold and Arid Regions Environmental and Engineering Research Institute, Chinese Academy of Sciences, Lanzhou 730000, China*
[d] *Key Laboratory of Environment Change and Resources Use in Beibu Gulf, Ministry of Education, Nanning Normal University, Nanning 530001, China*
[e] *School of Geography and Planning, Nanning Normal University, Nanning 530001, China*

ARTICLE INFO

ABSTRACT

The peak photosynthesis timing (PPT) is a key factor that affects the seasonality of the terrestrial carbon uptake. Carbon phenology derived from gross primary production (GPP) has been used to validate the peak greenness timing (PGT) from satellite-based vegetation indices (VIs) in phenology research. However, PPT, derived from GPP, has not been comprehensively analyzed, especially taking different GPP estimates, fitting methods, and biomes into account. Moreover, whether or not the PPT trend is consistent with the reported PGT trend still unclear. We explored the above questions at widely used flux sites in Northern Hemisphere mid-latitudes and found that no significant differences in PPT derived from GPP using different carbon flux partitioning methods. Moreover, fitting methods performed well in grassland, cropland, wetland, and wood savannas compared with evergreen needleleaf forest, deciduous broadleaf forest, and mixed forest. Unexpectedly, we did not find an advancing trend in PPT derived from GPP compared with PGT from SPOT-VGT normalized difference vegetation index (NDVI). Our study suggests that the principle of the fitting method and physiological property of the biome should be taken into account when predicting PPT. More importantly, PGT is not a good proxy of the PPT. Therefore, PPT trends based on VIs should be viewed with caution. In general, this study is meaningful for better understanding photosynthesis and carbon cycling in the context of changing climate.

1. Introduction

Phenology controls the seasonality of numerous ecosystem processes and affects interactions between the atmosphere and the biosphere (Piao et al., 2006; Richardson et al., 2018; Wu et al., 2013). In comparison with traditional and well-studied phenological measures, such as the start of the growing season (SOS), the end of the growing season (EOS), and the length of the growing season (LOS); peak photosynthesis timing (PPT) has only recently begun to receive attention in the phenological research community (Gonsamo et al., 2018; Chen et al., 2019; Wang and Wu, 2019; Yang et al., 2019). Changes in PPT could significantly impact the seasonality of terrestrial carbon cycling (Xu et al., 2016). PPT is closely related to annual gross primary production

(GPP) (Gonsamo et al., 2018; Li et al., 2020) and can indicate the timing of maximum resource availability; for example, the PPT for grassland corresponds to the timing of maximum forage, which affects habitat and the number of livestock (Paruelo et al., 2001; Wang et al., 2012; Yang et al., 2019). Accurate estimation of PPT is therefore helpful for predicting vegetation response to climate change, and then deepening our understanding of the carbon cycle in the context of a changing climate.

PPT is generally defined as the day that corresponds to the maximum value on a fitted vegetation index curve (Gonsamo et al., 2013). Previous studies have used vegetation indices (VIs) from different sources of remote sensing data and different fitting methods to determine the peak greenness timing (PGT), and consider PGT as a surrogate of PPT in trending and attributing analysis. For example, Xu et al. (2016) selected

the normalized vegetation difference index (NDVI) from the Global Inventory Modeling and Mapping Studies (GIMMS) product of the Advanced Very High Resolution Radiometer (AVHRR) and the Moderate Resolution Imaging Spectroradiometer (MODIS), and applied four commonly-used fitting methods: polynomial fitting (PN) (Cong et al., 2012; Piao et al., 2006), linear interpolation, spline smoothing, and interpolation (Forkel et al., 2015; Migliavacca et al., 2011), and singular spectrum analysis (Guan, 2014; Chen et al., 2019) to obtain PPT for Northern Hemisphere mid-latitudes. Gonsamo et al. (2018) proposed a double logistic function (DL) and used 34 years of GIMMS NDVI data to derive PPT for extratropical latitudes (> 23° N). To analyze PPT for China's ecosystems, Wang and Wu (2019) also used GIMMS NDVI, and designed the SG-cubic spline method that integrates the Savitzky-Golay filter (SG) (Jönsson and Eklundh, 2002) and cubic spline. Yang et al. (2019) developed a new PPT model that depends on the SG and on a generalized additive model, and used a Vegetation Photosynthesis Model (VPM)-based GPP and enhanced vegetation index (EVI) to compare PPT for temperate and alpine grassland regions in China. In general, previous studies based on VIs from remote sensing data have shown that PPT has a generally advancing trend.

Due to a lack of ground-based observations, PPT derived from remote sensing data is usually validated using PPT derived from tower flux GPP (Chen et al., 2019; Wang and Wu, 2019; Xu et al., 2016; Yang et al., 2019; Ge et al., 2021). In previous studies, GPP from one partitioning method is chosen from the FLUXNET2015 dataset as input data, and have used a variety of fitting methods to smooth daily tower flux GPP; for example, a moving averaging filter (MA) (Wang et al., 2019), SG (Xu et al., 2019), cubic smoothing spline (CS) (Wang et al., 2018; Wu et al., 2014), PN fitting (Xu et al., 2016), asymmetric Gaussian (AG) fitting (Jones et al., 2012), and DL (Gonsamo et al., 2013; Yang and Noormets, 2021). Using different input data and fitting methods may result in different PPT patterns being derived, and the differences may be great enough to result in contrary PPT trends. It is therefore important that PPT estimates derived from tower flux GPP are available to support the conclusions of satellite-derived PPT trends at different scales and biomes.

However, there are several uncertainties in previous studies. First, how the PPT is affected by uncertainties, which is resulted from complicated carbon data processing, is neglected by previous studies. Different carbon flux processing methods can lead to uncertainties in not only magnitude but also the seasonality of carbon flux. Second, only one fitting method is used to smooth the daily GPP and extract PPT in most previous studies. The performance of different fitting methods in deriving PPT across different biomes is still unclear. Third, it is not clear if the PPT trend derived from tower flux GPP is consistent with results from VIs. Therefore, our study employed four GPP estimates and six fitting methods, to extract PPT, and then compared the trend consistency of PPT and PGT. The objectives of this research are: (1) to investigate the effects of different GPP estimates in PPT extraction. (2) to assess the potential of different fitting methods for PPT detection at widely distributed flux sites that represent typical biomes. (3) to check whether or not the GPP-based PPT trend is consistent with that derived from remote sensing data.

2. Data and methods

2.1. GPP from flux sites

In this study, we used daily GPP at 48 eddy covariance (EC) sites (totally, 510 site-years) in the FLUXNET2015 dataset (https://fluxnet.org/data/download-data/) (Fig. 1). GPP is partitioned according to net ecosystem exchange (NEE) combining auxiliary meteorology data, following a process that is described in detail in Pastorello et al. (2020). A variable USTAR threshold (VUT) and a constant USTAR threshold (CUT) are used in NEE uncertainty calculation to avoid problems associated with false interannual variability signals, and with environmental change that could not be represented. Based on VUT and CUT, 40 NEE percentiles were calculated; and we followed Pastorello et al. (2020) in assuming that the "REF" version is generally the most representative. GPP is partitioned from NEE using two methods: the nighttime fluxes method (NT), and the daytime fluxes method (DT). In the NT method, nighttime data is used to parameterize a respiration (RECO) estimation model. In the DT method, both daytime and nighttime data are used to parameterize a two-component model. A USTAR threshold, the representativeness of the GPP data, and the partitioning method were taken into account and four GPP estimates (GPP_NT_CUT_REF, GPP_NT_VUT_REF, GPP_DT_CUT_REF, GPP_DT_VUT_REF) were chosen as the input data for PPT extraction. To ensure the quality of GPP data from different flux towers, we selected and filtered flux sites following Wang et al. (2019). For each site, we considered the data quality control (QC) for every site-year (QC > 0.75), the number of years of available data (at least 7 high-quality site-years were required), the spatial representativeness of the site, the seasonality of vegetation, and the biomes present at the site. Finally, the 48 selected sites were sorted into 7 types: grassland (GRA), cropland (CRO), deciduous broadleaf forest (DBF), and evergreen needleleaf forest (ENF), mixed forest (MF), wetland (WET), and woody savannas (WSA). The number of sites for each biome was: 5 GRA sites (site-years = 43), 7 CRO sites (site-years = 65), 12 DBF sites (site-years = 126), 16 ENF sites (site-years = 189), 5 MF sites (site-years = 65), 2 WET sites (site-years = 15), and 1 WSA site (site-years = 7). The earliest site-year is 1998 and the latest site-year is 2014 for the 48 sites. Details of selected sites could be found in supplementary Table S1.
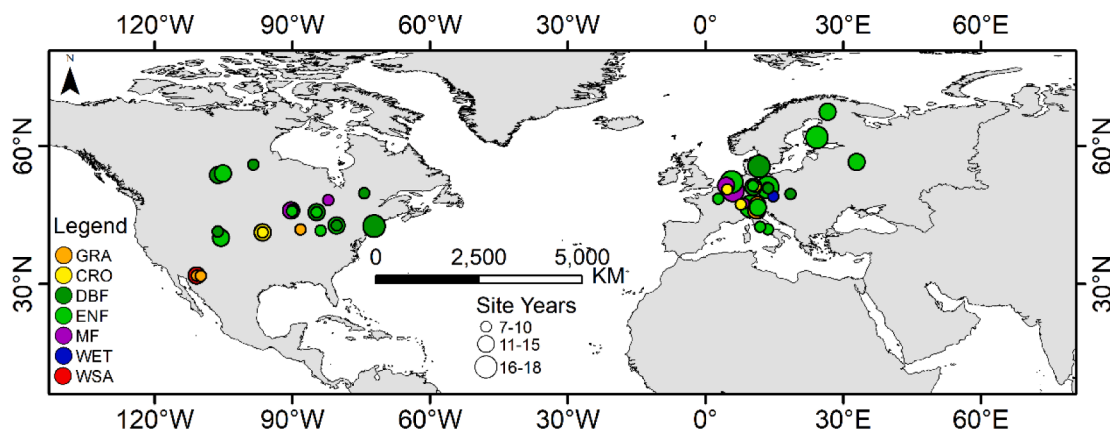

Fig. 1. Spatial distribution of flux sites used for this study. GRA, CRO, DBF, ENF, MF, WET, and WSA represent grassland, cropland, deciduous broadleaf forest, evergreen needleleaf forest, mixed forest, wetland, and woody savannas sites, respectively (see supplementary table for details).

2.2. NDVI from SPOT-VGT

As NDVI-based PGT (i.e., potential PPT) has been taken as a proxy of actual PPT in previous studies, we chose NDVI from SPOT-VGT to derive potential PPT in this study. NDVI time-series were downloaded from the SPOT-VGT S10 product (https://www.vito-eodata.be/PDF/datapool/), which has a temporal resolution of 10 days and a spatial resolution of 1 km. This product has been systematically corrected for topographic and atmospheric effects. NDVI for each flux site was obtained by following Wu et al. (2017) to obtain NDVI for each flux site. To match the earliest and latest site-year of the tower flux GPP, we calculated the daily average SPOT-VGT NDVI from 1999 to 2013 and used the calculated daily NDVI to fill the data gap for January to March 1998 and June to December 2014.

2.3. Method for dividing growing seasons

Some biomes (e.g., GRA and CRO) are likely to be experienced two or more growing seasons (GSs) in a calendar year. To accurately estimate the PPT for these biomes, it is vital to divide the observed total GSs for these biomes before deriving PPT (Kong et al., 2020). In this study, we developed a simple and effective method to divide the total GSs for GRA and CRO. The key to this method was that a single and complete GSs consists of two troughs and one peak. To balance fidelity and fitness when fitting the raw data, we compared six different fitting methods and selected the CS method as the most appropriate for fitting the raw GPP time-series (Figs. S1–S2). Fig. 2 is an example of GSs dividing at CH-Oe2 (a CRO site) in 2007, 2008, and 2009. To examine the accuracy of our approach, we compared the GSs dividing results to the detailed crop records of CH-Oe2 in Emmel et al. (2018). The details of the GSs dividing method implemented here are (Fig. 2):

Step 1: Identify all peaks and troughs on the fitted GPP time-series (orange and light blue dots) using a 30-day moving window. Through this, we obtained a dataset of potential peaks and troughs (dataset$_{peak\_trough}$).
Step 2: Remove adjacent peaks or troughs. If two peaks or troughs are adjacent, then a comparison will be triggered. The peak with the smaller GPP and the trough with the larger GPP will be removed.

Step 3: Remove troughs with GPP larger than GPP$_{trough}$ and repeat step 2.
Step 4: Judge whether each peak is reasonable on a peak-by-peak basis. We used the distance between two peaks ($|\Delta t_{peak}|$), the distance between a peak and the nearest two troughs ($|\Delta t_{peak\_trough\ (left)}|$ and $|\Delta t_{peak\_trough\ (right)}|$), and the GPP difference between the peak and the nearest troughs ($|\Delta GPP_{peak\_trough\ (left)}|$ and $|\Delta GPP_{peak\_trough\ (right)}|$) to judge whether to accept a peak. If not accepted, the peak was removed from dataset$_{peak\_trough}$, and step 2 was repeated. If one peak constituted the first element in dataset$_{peak\_trough}$ after every assessment, then it was also removed.
Step 5: Judge the length of a GSs. The length of a complete GSs ($|\Delta t_{trough}|$) was determined from two troughs. If $|\Delta t_{trough}|$ was less than one month, then the trough with larger GPP was removed from dataset$_{peak\_trough}$. Step 2 was then repeated.

2.4. Fitting methods

When deriving phenological information fromtime-series of satellite data or tower flux GPP, the initial step is to fit a smooth time-series to the raw input data. In this study, we chose six widely-used fitting approaches and grouped them into two categories: local fitting functions, which were MA, SG, and CS, and global fitting functions, which were PN, AG, and DL. We fitted GPP time-series using different approaches in R language.

2.4.1. MA

The MA fitting function uses a moving window to calculate an average. The weight for each point within the window is calculated from a Gaussian density function: it is highest in the middle of the window and decreases at the two sides. In this study, we used a 15-day moving window for our moving average filter, following Wang et al. (2019).

2.4.2. SG

The SG method is commonly used in signal processing and has been integrated into various models and software (Chen et al., 2004; Jönsson & Eklundh, 2002; Xu et al., 2019; Yang et al., 2019). The SG incorporates a moving window and a quadratic PN to obtain the fitted value in a window (Jönsson and Eklundh, 2002), as described in Eq. (1):
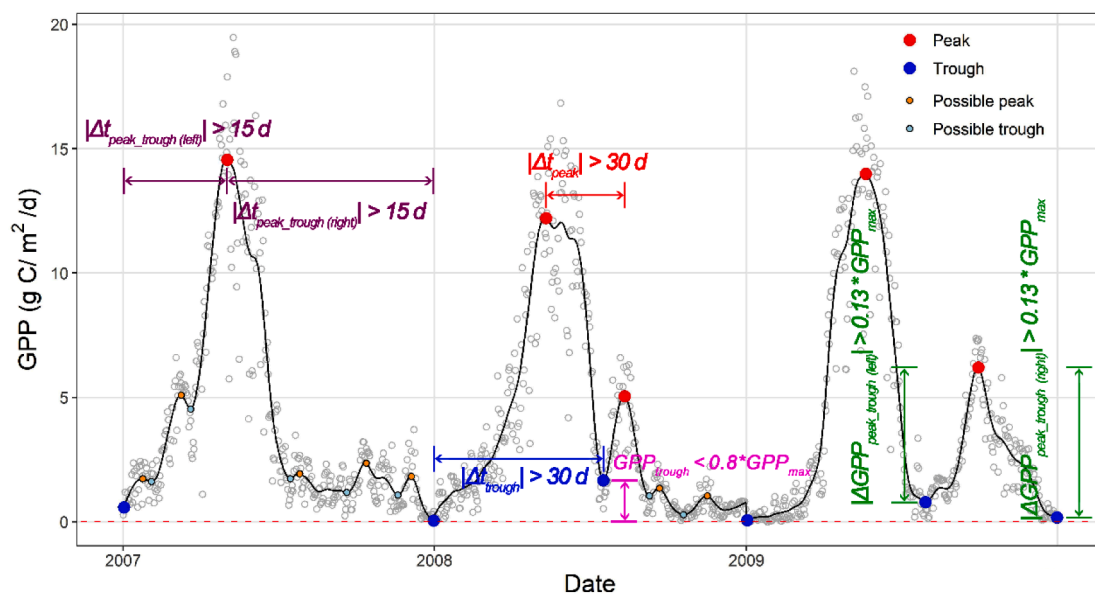

Fig. 2. An example of dividing growing seasons at the CH-Oe2 (a cropland site) in 2007, 2008, and 2009. The grey circle denotes raw daily gross primary production (GPP). The orange and light blue dots represent possible peaks and troughs, respectively. The red and blue dots indicate peaks and troughs that were accepted as reasonable following the steps outlined in the text.

$$GPP_i^* = \frac{\sum_{i=-m}^{m} C_i GPP_{j+i}}{2m+1} \tag{1}$$

where GPP^* is the smoothed GPP, m is the half of smoothing window, and C_i is the weight assigned to the daily GPP data point within the smoothing window. Our study set the smoothing window size to 30, following Bórnez et al. (2020).

2.4.3. CS

The CS method uses the locally weighted regression principle to fit noisy data and generates a smooth time-series for an entire period. It is regarded as a flexible approach to time-series fitting (Chen et al., 2006). For example, CS is used in the processing of the MODIS phenology product MCD12Q2. The GPP for a given date can be calculated from data for the two adjacent dates (e.g., (t_i, y_i) and (t_{i+1}, y_{i+1})), using the following formula:

$$S_i(t) = a_i(t-t_i)^3 + b_i(t-t_i)^2 + c_i(t-t_i) + d_i \tag{2}$$

where S_i is a cubic polynomial, t is a date (DOY), and a_i, b_i, c_i, d_i are coefficients.

2.4.4. PN

Polynomial fitting is also a practical approach and has been used in many phenology studies. For example, Piao et al. (2006) and Xu et al. (2016) employed a six-degree PN and a least-squares regression to remove noise from time-series. In general, seasonal GPP data may be smoothed using an inverted parabola of the form below:

$$GPP = \beta + \beta_1 t + \beta_2 t^2 + \beta_3 t^3 + a\beta_4 t^4 + \beta_5 t^5 + \beta_6 t^6 \tag{3}$$

where t is a date (DOY), and β and β_{1-6} are the coefficients of a sixth-order polynomial.

2.4.5. AG

The AG method is a global fitting model based on several local functions, and the fitted curve can reflect complex and subtle changes in the data (Jönsson and Eklundh, 2002). The local function can be expressed in the following form:

$$f(t) = c_1 + c_2 g(t; \theta_1, \ldots, \theta_5) \tag{4}$$

$$g(t; \theta_1, \ldots, \theta_5) = \begin{cases} exp\left[-\left(\dfrac{t-\theta_1}{\theta_2}\right)^{\theta_3}\right], & \text{if } t > \theta_1 \\ exp\left[-\left(\dfrac{\theta_1-t}{\theta_4}\right)^{\theta_5}\right], & \text{if } t < \theta_1 \end{cases} \tag{5}$$

where Eq. (5) is a Gaussian function and c_1, c_2 are linear parameters that determine the base level and amplitude, respectively; θ_1 determines the position of extremes for time variable t; θ_2, θ_3 are related to the width and fatness of the left part of the function; and θ_4, θ_5 are related to the width and fatness of the right part of the function. The left and right asymmetric Gaussian can be integrated using $f(t)$. The global fitting function is described in Eq. (6):

$$F(t) = \begin{cases} \alpha(t)f_L(t) + [1-\alpha(t)]f_C(t), & t_L < t < t_C \\ \beta(t)f_C(t) + [1-\beta(t)]f_R(t), & t_C < t < t_R \end{cases} \tag{6}$$

where α, β are cutoff functions and f_L, f_C, and f_R are the left minimum, central maximum, and right minimum, respectively, for a calculated interval. t_L, t_R, t_C are the times that correspond to f_L, f_C, f_R

2.4.6. DL

The DL fitting approach is structurally flexible and can provide good coverage (Yang and Noormets, 2021). DL has been developed and optimized in previous studies (Elmore et al., 2012; Gu et al., 2009; Klosterman et al., 2014; Zhang et al., 2005). In this study, we used a DL

with seven parameters from Gu et al. (2009), following Yang and Noormets, (2021), as described in Eq. (7):

$$GPP(t) = m_0 + \frac{m_1}{\left(1 + e^{-n_1(t-t_1)}\right)^{k_1}} - \frac{m_2}{\left(1 + e^{-n_2(t-t_2)}\right)^{k_2}} \tag{7}$$

where t is the date (DOY); m_0, m_1, m_2 correspond to the GPP values for the dormant period, for early summer, and for later summer, respectively; n_1, n_2 are two slope coefficients; and k_1, k_2 are two transition dates.

2.5. Analysis

2.5.1. Measurement of plateau length

To measure the plateau length of each biome and its impact on the PPT, we introduced the length of the peak (LOP) proposed by Gonsamo et al. (2013). LOP is the difference between the start of the peak (SOP) and the end of the peak (EOP). SOP and EOP could be obtained on the rising and falling parts of the fitted GPP curve using a certain threshold (Fig. S3).

2.5.2. Fit evaluation

In our study, we used five statistics to evaluate the performance of the different fitting methods. The first was the coefficient of determination (R^2), as described in Eq. (8):

$$R^2 = \frac{\Sigma_{t=1}^{n}(GPP_o(t) - \overline{GPP_o})^2 \Sigma_{t=1}^{n}\left(GPP_o(t) - GPP_p(t)\right)^2}{\Sigma_{t=1}^{n}(GPP_o(t) - \overline{GPP_o})^2} \tag{8}$$

where GPP_o and GPP_p are observed and predicted GPP values, respectively. $\overline{GPP_o}$ is the annual mean observed GPP, and n is the number of available observations in one year.

The second statistic was the root mean square error (RMSE), as described in Eq. (9):

$$RMSE = \sqrt{\frac{\sum_{t=1}^{n}\left(GPP_o(t) - GPP_p(t)\right)^2}{n}} \tag{9}$$

The third statistic was the empirical bias, which was used to calculate the mean error for the residuals of each fitting method, as described in Eq. (10):

$$Bias = \frac{\sum_{t=1}^{n}\left(GPP_o(t) - GPP_p(t)\right)}{n} \tag{10}$$

The fourth statistic we considered was the agreement index (AI), which is frequently used for model assessment, and was used here to estimate the relative error of a fit (Gu et al., 2002; Zhou et al., 2016). AI ranges from 0 to 1, and a higher value means a better fit. It is described in Eq. (11):

$$AI = 1 - \frac{\sum_{t=1}^{n}\left(GPP_o(t) - GPP_p(t)\right)^2}{\sum_{t=1}^{n}\left(|GPP_p(t) - \overline{GPP_o}| + |GPP_o(t) - \overline{GPP_o}|\right)^2} \tag{11}$$

The fifth statistic was Akaike's Information Criterion (AIC), which is employed to evaluate the performance of fitting methods with different free parameters (Atkinson et al., 2012). AIC is calculated using Eq. (12).

$$AIC = 2k + n[ln(RSS)] \tag{12}$$

where, k is the number of free parameters in the fitting method, n is the number of input data, RSS is the residual sum of squares between the original and fitted data. A lower AIC indicates the method is preferable.

2.5.3. Analysis of variance

To compare the performance of different fitting methods and GPP estimates for deriving PPT, we used analysis of variance (ANOVA) to analyze the differences between the group means. ANOVA provides a statistical test for more than two groups of data, regardless of whether

the means of the different groups are equal or not. If there is no significant difference between the two groups' means, then the same lowercase letter is assigned to these two groups. Otherwise, two different lower-case letters are assigned to the two groups.

2.5.4. Trend test

Mann-Kendall (MK) test was employed to examine the trends in phenology and environmental variables (Mann et al., 1945; Kendall et al., 1948). MK test is widely used in trend analysis with multiple advantages. For example, MK test is a nonparametric test and does not assume a specific distribution for the data. Moreover, it is not sensitive to outliers. The Theil-sen method was used to estimate the slope of the MK test (Sen et al., 1968). These statistical analyses were carried out using the R language.

3. Results

3.1. PPT from different GPP estimates

To assess whether different GPP estimates lead to differences in PPT prediction, we analyzed the correlations between PPT values calculated from four different GPP estimates (Fig. 3). In general, PPT values calculated from different GPP estimates were significantly correlated ($p < 0.001$), although the correlation coefficient (R) varied with the fitting method. The results also suggested that PPT values that were calculated from the same partitioning methods, but using different USTAR thresholds, were more strongly correlated than PPT values that were calculated from different partitioning methods and different USTAR thresholds. For example, R for the correlations between PPT values

calculated from the same partitioning method (DT_CUT vs. DT_VUT and NT_CUT vs. NT_VUT) were 0.88 and 0.95, while the R was lower between PPT values that were calculated using different partitioning methods and different USTAR thresholds (e.g., DT_CUT vs. NT_CUT or DT_CUT vs. NT_VUT) (Fig. 3a). We used ANOVA to compare the means of the PPT values calculated using different GPP estimates (Fig. 4). No significant difference was found between the PPT values that were calculated using the four different GPP estimates.

3.2. PPT values calculated using different fitting methods

We first compared PPT estimates using the local and global fitting methods and found that PPT estimates based on global fitting methods were generally more centralized than PPT estimates based on local fitting methods (Fig. 3). Results from ANOVA, which used Duncan's multiple range test, suggested that the appropriateness of different fitting methods may vary significantly between different biomes (Fig. 3 and Fig. 5). There was no significant difference between the PPT estimates using different local fitting methods for any biome. There were also no significant differences between the PPT estimates that were made using the six different fitting methods for the GRA, CRO, and WSA biomes. However, there were significant differences between these PPT estimates from the PN and the DL for DBF, ENF, and MF biomes. PPT estimates made using PN to fit the data were significantly different from PPT estimates that were made using the three local fitting methods, and there was a significant difference between PPT derived using PN and PPT that was derived using the other two global fitting methods for DBF. For all biomes, the mean PPT that was estimated using PN was later than the mean PPT estimated using the other fitting methods. The standard
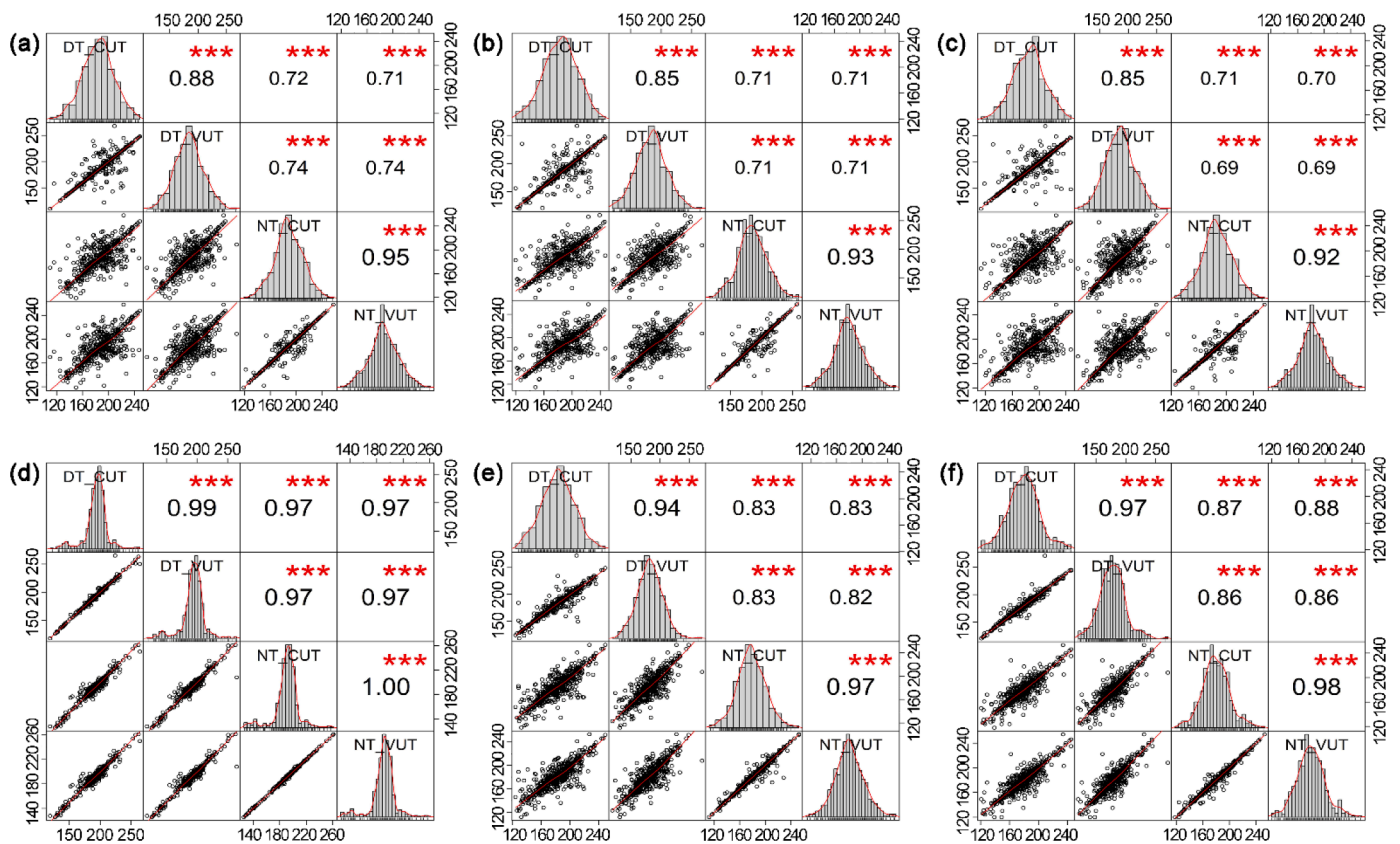

Fig. 3. Correlations between the peak photosynthesis timing (PPT), as calculated using four different gross primary production (GPP) estimates and six different fitting methods. (a) Moving average filter, (b) Savitzky-Golay filter, (c) Cubic smoothing spline, (d) Polynomial, (e) Asymmetric Gaussian, and (f) Double logistic function. DT_CUT, DT_VUT, NT_CUT, and NT_VUT are four different GPP estimates, corresponding to GPP_DT_CUT_REF, GPP_DT_VUT_REF, GPP_NT_CUT_REF, GPP_NT_CUT_REF, respectively. One dot represents PPT from two different GPP estimates. Three asterisks show that there is a significant correlation ($p < 0.001$) between the PPT values calculated from two different GPP estimates.
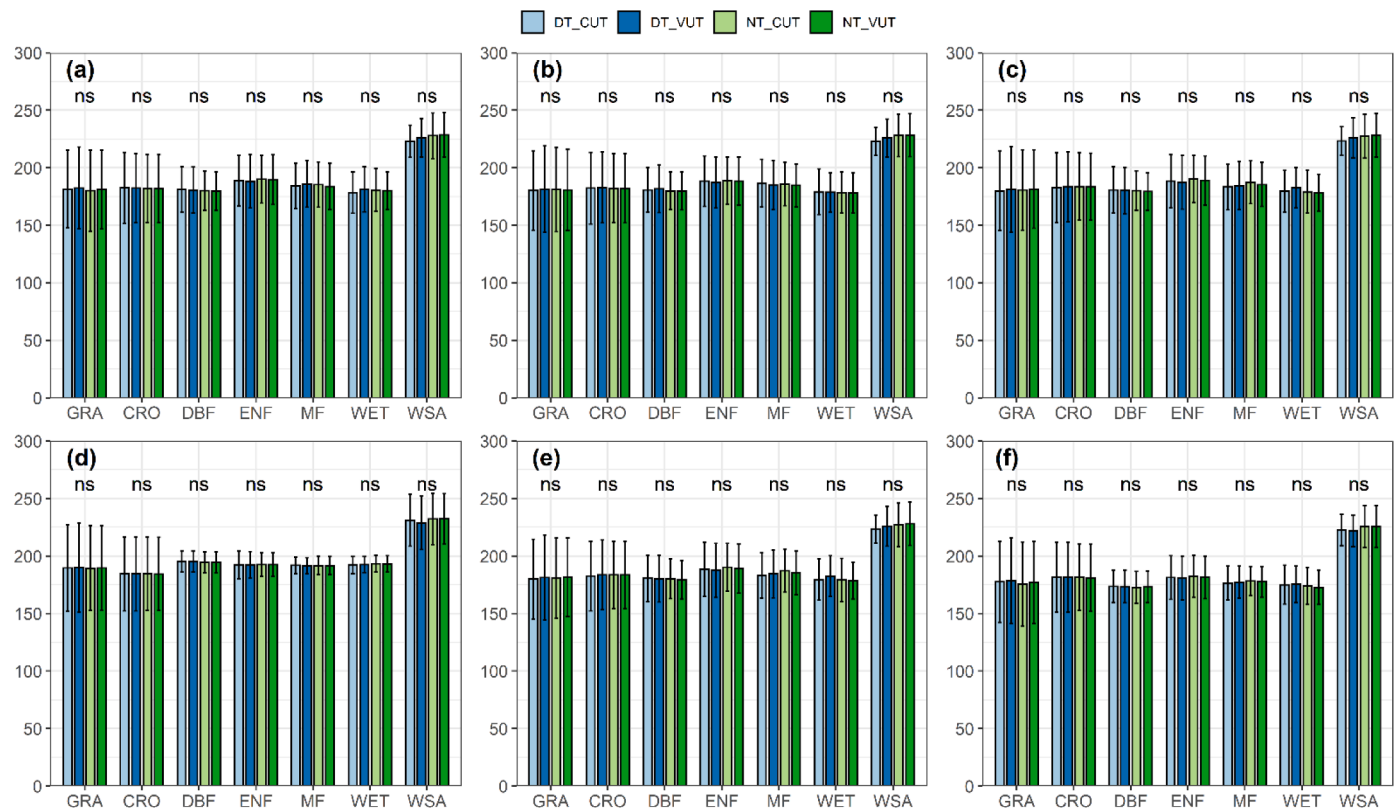
Fig. 4. Comparison of the peak photosynthesis timing (PPT) calculated from four different gross primary production (GPP) estimates using analysis of variance (ANOVA). (a) Moving average filter, (b) Savitzky-Golay filter, (c) Cubic smoothing spline, (d) Polynomial, (e) Asymmetric Gaussian, and (f) Double logistic function. DT_CUT, DT_VUT, NT_CUT, and NT_VUT are four different GPP estimates, corresponding to GPP_DT_CUT_REF, GPP_DT_VUT_REF, GPP_NT_CUT_REF, GPP_NT_VUT_REF, respectively. GRA: grassland, CRO: cropland, DBF: deciduous broadleaf forest, ENF: evergreen needleleaf forest, MF: mixed forest, WET: wetland, WSA: woody savannas. The lower-case letters from ANOVA show whether or not there is a significant difference between the different PPT values. Error bars show the standard deviation.

deviation (SD) of PPT estimates resulting from the global fitting methods (PN, AG, DL) was smaller than the SD of estimates calculated using the local fitting method (MA, SG, CS) for the DBF, ENF, and MF biomes. The SD was lower for PPT estimates that were based on PN than for estimates based on any of the other three global fitting models.

We found substantial differences in the PPT estimated for different biomes in our study. For all biomes, PPT calculated using PN was later than that calculated using other methods, particularly in the GRA, CRO, DBF, MF, and WET biomes (Figs. 5 and 6). The earliest PPT (the lower whisker) was around day 120, and the latest PPT (the upper whisker) was around day 270. The range of PPT estimates (the length of the box) was wider for the GRA, CRO biomes than for the other biomes. PPT estimates for GRA had a distinct right-skewed distribution, indicating that the mean of PPT estimates were later than the median. The distribution of PPT estimates for CRO was left-skewed, suggesting that the mean of PPT estimates for the CRO biome were earlier than the median (Fig. 6). There were more outliers in the distributions of PPT estimates for the DBF and ENF biomes than for the other biomes. Outliers in the distribution for the DBF biome were mostly located above the maximum, while outliers for the distributions in the ENF biome were located below the minimum (Fig. 6).

3.4. PPT trends

We first explored the PPT trends from six different fitting method for each site (Fig. 7). In general, we found that the PPT trends were relatively consistent for most of selected site (at least four of the six estimated trends were consistent), except for few sites. We excluded the WET and WSA biomes from this analysis as there were only one or two

sites that represented these. We then compared the PGT and PPT trend for all used sites (Fig. 8). When MA was used, 19 (39.58%) sites showed an advancing PPT trend, although none of these was significant ($p <$ 0.05), and 29 (60.42%) sites showed a delaying trend, and two of these trends were significant. Results for the SG and CS methods were similar to those for the MA method. The numbers of sites with an advancing trend were 15 (31.25%) and 18 (37.50%) for SG and CS, respectively; and most of the sites showed a delaying trend. In general, PPT trends that were estimated using one of the three local fitting methods showed a delaying trend. For PN, AG, and DL, the numbers of sites with an advancing estimated PPT trend were 23 (47.92%), 24 (50%), 21 (43.75%), respectively. Only one or two flux sites showed a significant advancing trend. For PPT trends estimated using PN and AG, the proportion of advancing and delaying trends was almost equal. We also calculated the PGT trends using SPOT-VGT NDVI at the same flux sites. Interestingly, we found an advancing PGT trend using NDVI at the site scale (Fig. 8), which was consistent with previous studies based on VIs.

4. Discussion

4.1. Impact of different GPP estimates

In the phenology studies, GPP from flux tower plays an important role in validating results from remote sensing data. GPP data are particularly important when there are no ground phenological observations such as PPT. Therefore, PPT estimates derived from tower flux GPP are often used to validate results derived from remote sensing data (Gonsamo et al., 2018; Li et al., 2020; Wang and Wu, 2019; Xu et al., 2016). However, there are 40 different GPP estimates in the
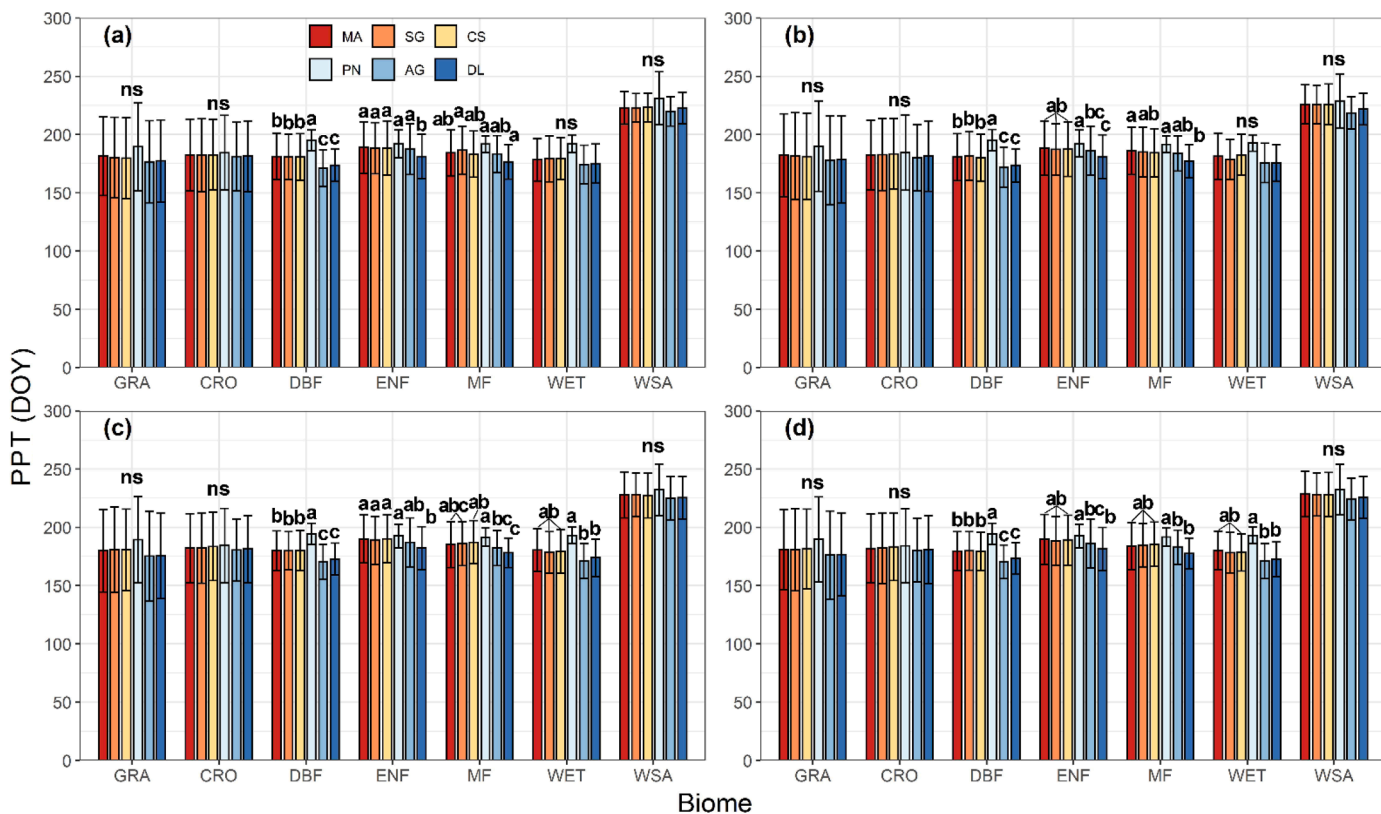
Fig. 5. Analysis of variance (ANOVA) comparison of estimates of the peak photosynthesis timing (PPT) that were calculated using six different fitting methods. (a) GPP_DT_CUT_REF, (b) GPP_DT_VUT_REF, (c) GPP_NT_CUT_REF, (d) GPP_NT_VUT_REF. GRA: grassland, CRO: cropland, DBF: deciduous broadleaf forest, ENF: evergreen needleleaf forest, MF: mixed forest, WET: wetland, WSA: woody savannas. The lower-case letters from the analysis of variance (ANOVA) show where there is a significant difference between the PPT estimates. Error bars indicate the standard deviations.3.3 PPT for different biomes
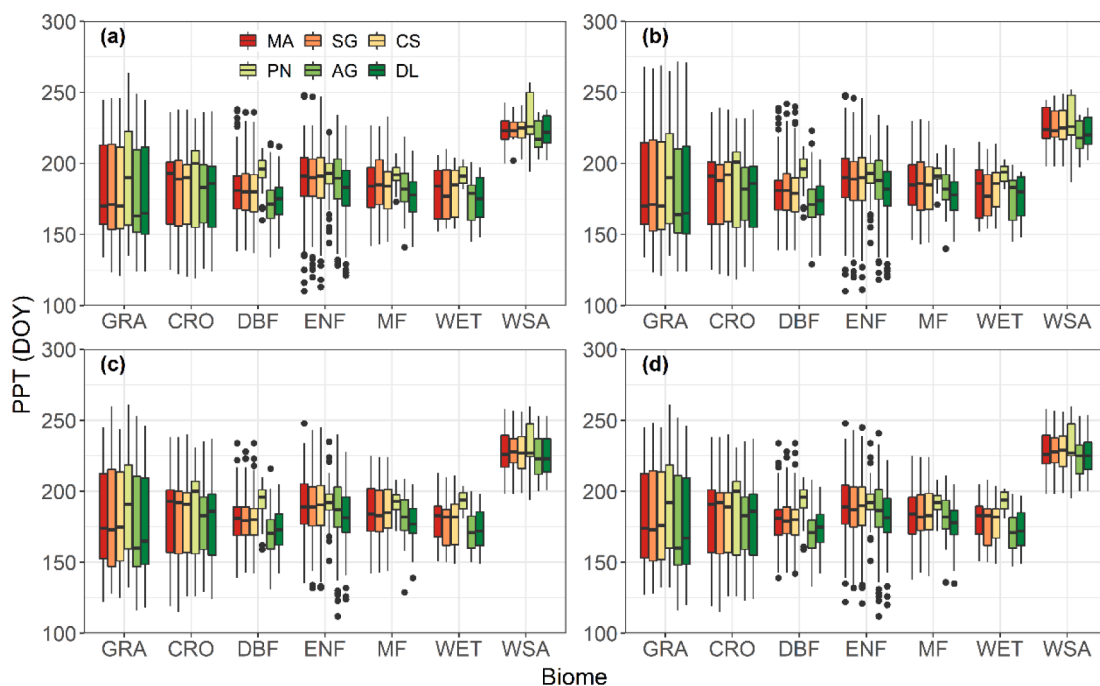

Fig. 6. The peak photosynthesis timing (PPT) for different biomes. (a) GPP_DT_CUT_REF, (b) GPP_DT_VUT_REF, (c) GPP_NT_CUT_REF, (d) GPP_NT_VUT_REF. GRA: grassland, CRO: cropland, DBF: deciduous broadleaf forest, ENF: evergreen needleleaf forest, MF: mixed forest, WET: wetland, WSA: woody savannas. MA, SG, CS, PN, AG, and DL represent the moving averaging filter, Savitzky-Golay filter, cubic smoothing spline, polynomial, asymmetric Gaussian, and double logistic function, respectively.
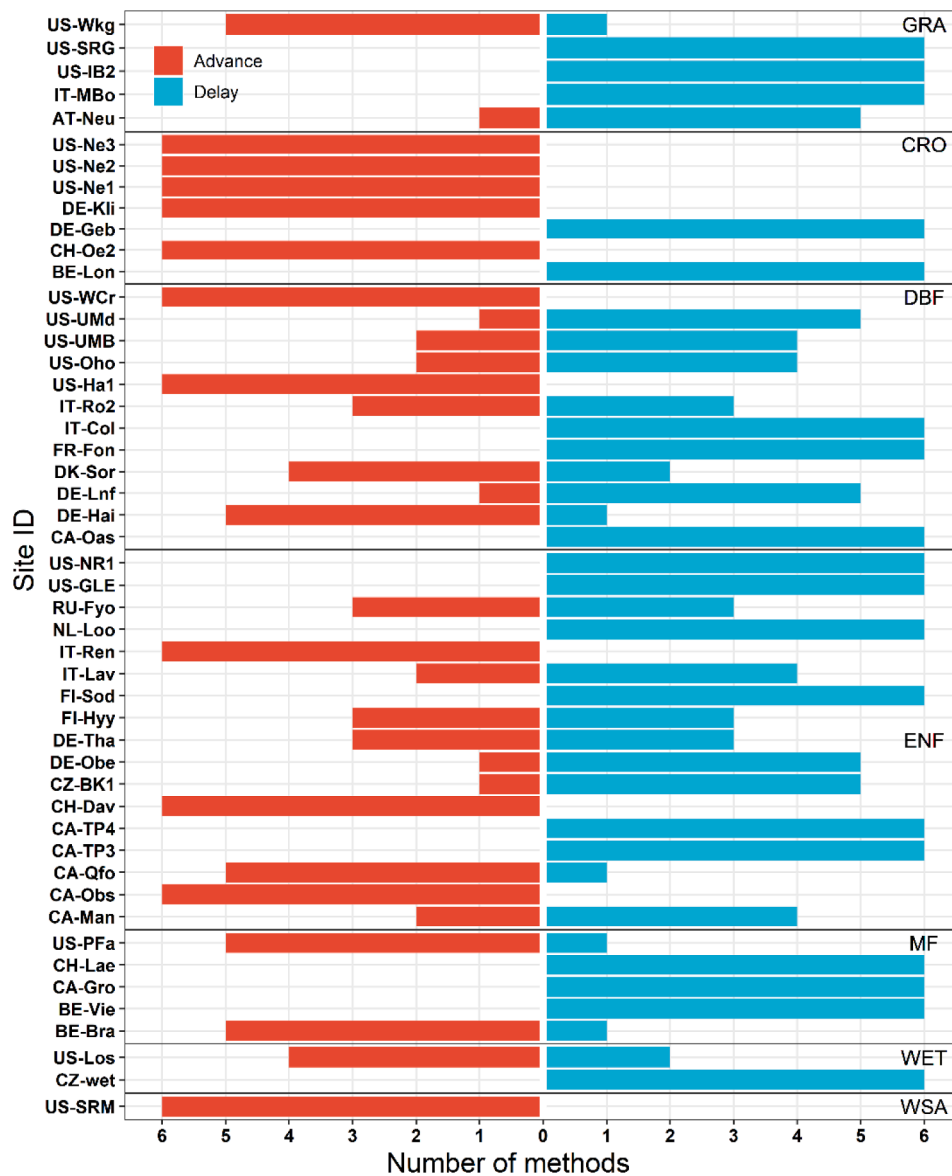
Fig. 7. The peak photosynthesis timing (PPT)trends from six fitting methods at used sites. GRA: grassland, CRO: cropland, DBF: deciduous broadleaf forest, ENF: evergreen needleleaf forest, MF: mixed forest, WET: wetland, WSA: woody savannas. This is an example using GPP_DT_CUT_REF.

FLUXNET2015 dataset (Pastorello et al., 2020).The impacts of different GPP estimates on the PPT and their trends, need to be compared. We chose four typical GPP estimates from the dataset (GPP_DT_CUT_REF, GPP_DT_VUT_REF, GPP_NT_CUT_REF, GPP_NT_CUT_REF), considering their representativeness and the partitioning method and the USTAR threshold that was used. We found that PPT estimates derived from GPP based on the same partitioning method but on different USTAR thresholds, were closely correlated. The coefficient of correlation decreased between PPT estimates that were derived from different partitioning methods and different USTAR thresholds (Figs. 3 and 6). In other words, different GPP estimates may lead to different PPT estimates being derived. We compared the means of the PPT estimates based on each of the different GPP estimates and did not find any significant differences (Fig. 4). In addition, we compared the PPT trends derived from different GPP estimates and found that there were no differences at different flux sites. Different partitioning methods and USTAR thresholds result in different GPP estimates, and this affects the PPT derived from the annual GPP time-series. However, different GPP estimates do not lead to different estimated PPT trends at each flux site.

4.2. Impact of different fitting methods

The first step in extracting phenological metrics from raw VIs observed by satellites or from GPP flux-tower measurements is to smooth the data, using one of a range of different fitting methods (Atkinson et al., 2012; Tian et al., 2021; Wang et al., 2017; Wang et al., 2017; Yuan et al., 2018). To evaluate the performance of different fitting methods for PPT estimation, we selected six commonly used fitting methods and divided them into local and global fitting methods. First, we evaluated the goodness of fit (GOF) for different fitting methods (Tables S2 and S3). We found fidelity was better for local fitting methods, while fitness was better for global fitting methods. Possible reasons are as follows: The local fitting methods reconstruct time-series in a given time window. For this reason, the local fitting method could preserve the local extremum and its position. The global fitting approaches merge multiple local functions to obtain a single fit and uses more free parameters to achieve a good fitness. Of the global fitting methods, PN resulted in a slightly weaker correlation between the fit and the GPP time-series than AG and DL did, as shown by R^2, which is consistent with findings from a previous study (Rodrigues et al., 2012).
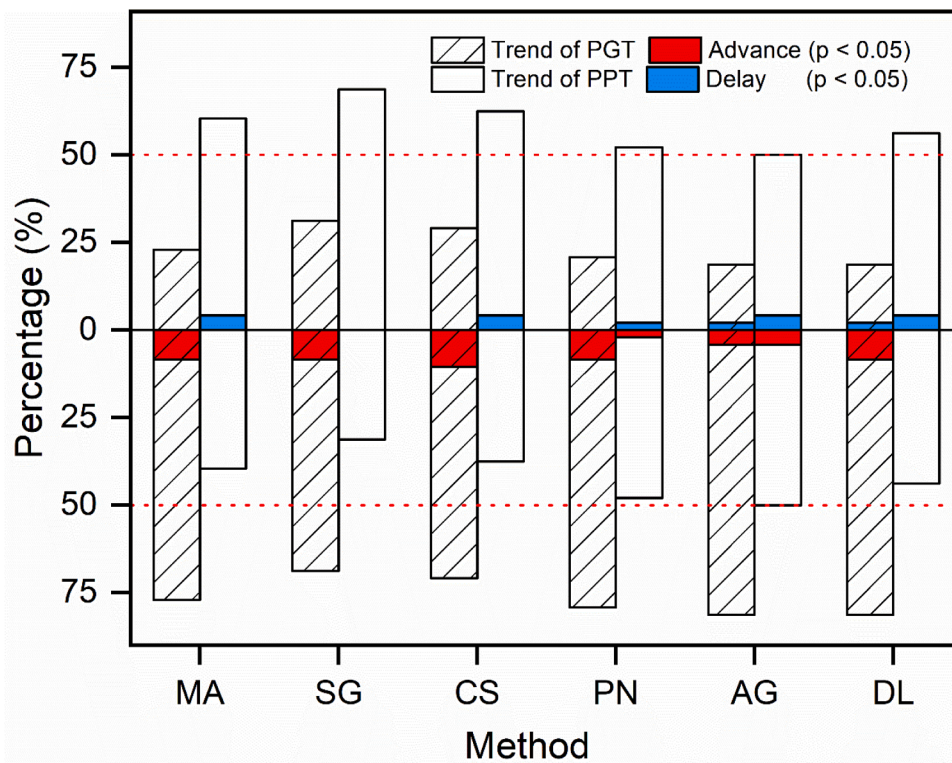
Fig. 8. The peak greenness timing (PGT) and peak photosynthesis timing (PPT) trends at selected flux sites. MA, SG, CS, PN, AG, and DL represent the moving averaging filter, Savitzky-Golay filter, cubic smoothing spline, polynomial, asymmetric Gaussian, and double logistic function, respectively. The bars below zero indicate the percentage of sites with advancing PPT/PGT trend estimates, and the bars above zero represent the percentage of sites with delaying PPT/PGT trend estimates. The red or blue colour indicates that the trend is significant ($p < 0.05$). The red dotted lines show where the estimated trend is significant for 50% of sites.

The bias was slightly higher for the AG and DL methods than for PN, which probably indicates that the predicted values deviated from the raw data to achieve a better global fit (Atkinson et al., 2012; Cai et al., 2017). In general, the AIC of DL was lower than that of AG and DL (Table S3). Secondly, we compared the PPT estimates derived from different fitting methods. In general, we found a wider range of PPT estimates resulted from the local fitting than from the global methods (Figs. 3 and 6). The local fitting approaches are more likely to preserve the position of local maxima (Jönsson and Eklundh, 2002, 2004), and the estimated PPT may reflect fluctuations in the original GPP estimate. This effect can be seen in the higher standard deviations for PPT estimates resulting from three local fitting methods than for estimates from the global fitting methods (Fig. S5). PPT estimates from the PN fitting method were the most centralized (Fig. 3d) and were always later than the PPT estimates from the other five fitting methods in all biomes (Figs. 5 and 6). This may be related to the six-degree PN function, shaped like an inverted U, and is symmetric within an area near the maxima (Elinav et al., 2005; Wang et al., 2017). As a result of this shape, this method may not capture the variability of the original data peak. We found that the choice of different fitting methods significantly impacted the estimated PPT trend. Based on the above comparison, we considered DL was the most reliable fitting method in PPT extraction and following analyses.

4.3. Impact of different biomes

Phenological metrics derived from flux-tower measurements of GPP have been widely used for validating PPT estimates derived from remote sensing data (Gonsamo et al., 2012; Tang et al., 2015; Wu et al., 2012; Zhao et al., 2020), yet the potential of GPP to predict PPT varies substantially across different biomes. Differences in the physiological properties of different biomes may play a fundamental role in determining the potential of GPP for PPT modeling. The plateau length in the curve fitted to data for each biome may be the key physiological feature that affects PPT estimates. To analyze the relationship between PPT and plateau length, we first used LOP proposed by Gonsamo et al. (2013) to

measure the plateau length for different biomes. We found a larger LOP for the ENF, DBF, and MF biomes than for the GRA, CRO, WET, and WSA biomes. Deriving PPT from the curves of NDVI or GPP is different from the extraction of SOS or EOS. SOS and EOS are found on the rising and falling parts of the fitted curve, which are monotonic in shape (Li et al., 2017; Testa et al., 2018; Xiao et al., 2006; Zhang et al., 2005). PPT is detected in a plateau of the fitted curve, which is sensitive to fluctuations in the original data (Fig. S3). The LOP was greatest for the curve fitted for the ENF biome, followed by the curves for the DBF and MF biomes. The significantly different performance of the different fitting methods for PPT estimation showed that the larger LOP would lead to lower certainty in the PPT estimation (Figs. 5 and S5). The daily GPP data fluctuated more widely in the plateau part of the curve than in increasing and falling phases (Fig. S3). The plateau usually occurs in summer, and fluctuations may be attributable to variable photosynthetically active radiation (APAR) and/or to temperature (Schubert et al., 2010; Xiao et al., 2021; Xu et al., 2020). Outliers to the distributions for the ENF, DBF, and MF biomes also suggest that the plateau may be a critical physiological feature for PPT estimation (Fig. 6) since these biomes are associated with a long and fluctuating plateau, which makes PPT estimation less certain.

4.4. Differences in PGT and PPT

Structural VIs, for example, NDVI and EVI, have been widely employed to identify photosynthetic phenology in the last decade (Chang et al., 2019; D'Odorico et al., 2015; Gonsamo et al., 2012; Shen et al., 2014; Yin et al., 2020). In recent years, more and more trending and attributing research on PPT have relied on structural VIs (Gonsamo et al., 2018; Wang and Wu, 2019; Xu et al., 2016; Yang et al., 2019). However, whether the VIs-based PGT trend is consistent with tower flux GPP-based PPT trend has not been compared. We found an advancing PGT trend based on SPOT-VGT NDVI, consistent with previous studies based on NDVI (Gonsamo et al., 2018; Wang and Wu, 2019; Xu et al., 2016). However, the results from this study indicated that GPP-based PPT showed a delaying trend, which is contrary to previous studies

based on NDVI. The main possible reasons are as follows: (1) Premature saturation of NDVI in the early stage of peak season may be a critical reason to explain that GPP-based PPT is later than the NDVI-based PGT. The low correlation between NDVI-based PGT and GPP-based PPT in our previous study also indicates that NDVI-based PGT is not a good surrogate of GPP-based PPT when taking all biomes into account (Fig. 9). (2) Actual photosynthetic activity does not reach the peak when the canopy structure reaches maturity. Photosynthetic capability is closely related to leaf mass per area and leaf chlorophyll content, asynchronism exists in leaf development and photosynthesis capability (Gamon et al., 1995; Muraoka and Koizumi, 2005). In general, the mismatch and different trends between NDVI-based PGT and GPP-based PPT could be attributed to that VIs are more suitable for describing the ecosystem structure and canopy development rather than ecosystem activity. Furthermore, we explored the correlations between PPT and available environmental factors (i.e., average air temperature, accumulated incoming shortwave radiation, accumulated precipitation, average vapor pressure deficit, and average soil temperature in spring and summer) at each flux site (Figs. S7 and S8). The result suggested that summer air and soil temperature were two main controls and positively correlated with PPT. In addition, summer vapor pressure deficit was another important factor and negatively correlated with PPT. Our study suggested that the number of sites controlled by air and soil temperature was slightly more than that controlled by vapor pressure deficit. Moreover, air and soil temperature showed an increasing trend at more sites. We considered that rising temperature (soil and air temperature) contributed more to the delaying PPT. We believed that the delaying PPT was a complex question because it involves pre-season climatic factors, but also pre-season phenological indicators related to PPT (e.g., SOS). Therefore, more detailed physiological mechanisms should be discussed in the future.

4.5. Limitations and uncertainties

Carbon phenology data derived from flux-tower measurements are regarded as crucial validation data for results derived from remote sensing data. However, the quality of phenological metrics derived from tower flux GPP is not widely reported, and this is especially true for PPT. We systematically compared PPT estimates derived from four different

typical GPP estimates, using six different fitting methods, in seven different and widespread biomes to better ensure the robustness of our results. However, there remain some shortcomings in the current study. Firstly, we did not examine whether the rules used to calculate PPT affect the estimated PPT trend. In most previous studies, PPT has been considered to be the timing of the maxima on the fitted curve (Li et al., 2020; Park et al., 2019; Wang and Wu, 2019; Gonsamo et al., 2012; Yang et al., 2019). Wang et al. (2020) took the average of the times the fitted time-series crossed a threshold (e.g., 80%) on the rising and falling parts. TIMESAT, a widely-used software in phenology research, also took PPT to be the average of two specific phases (Jönsson and Eklundh, 2004). Secondly, it may be appropriate to reconsider the current definition of PPT so as to take the physiological properties of different biomes into account. For GRA and CRO, the present definition may be appropriate as there was a short plateau period on the fitted curve. Different fitting methods resulted in relatively consistent PPT estimates for these biomes in this study. For DBF and ENF, there was a long plateau on the fitted GPP curve, making it hard to determine which date should be regarded as the PPT for these biomes. It may be more rational to regard PPT as a period rather than a point on the fitted curve for these biomes. Thirdly, solar-induced chlorophyll fluorescence (SIF) may be a better surrogate for GPP in the PPT study. SIF and GPP both are physiological parameters of plants, and a strong correlation has been proved in multiple flux sites (Li et al., 2018). Lastly, the results in this study indicate that, to improve PPT estimates and optimize current models, more attention should be paid to the rules used to calculate PPT. For example, the physiological properties of different biomes should be accounted for, and the performance of present fitting approaches should be assessed.

5. Conclusion

PPT modeling using GPP from flux towers remains a challenge; however, this is crucial to understanding photosynthetic capability and validating results derived from remote sensing data. Our study provides several valuable findings. Firstly, different GPP estimates may affect the PPT for an individual year, but PPT trends derived from four different GPP estimates were consistent. Secondly, all the fitting methods resulted in consistent estimates of PPT for GRA, CRO, WET, and WSA.While, different fitting methods exhibited different and limited capabilities in
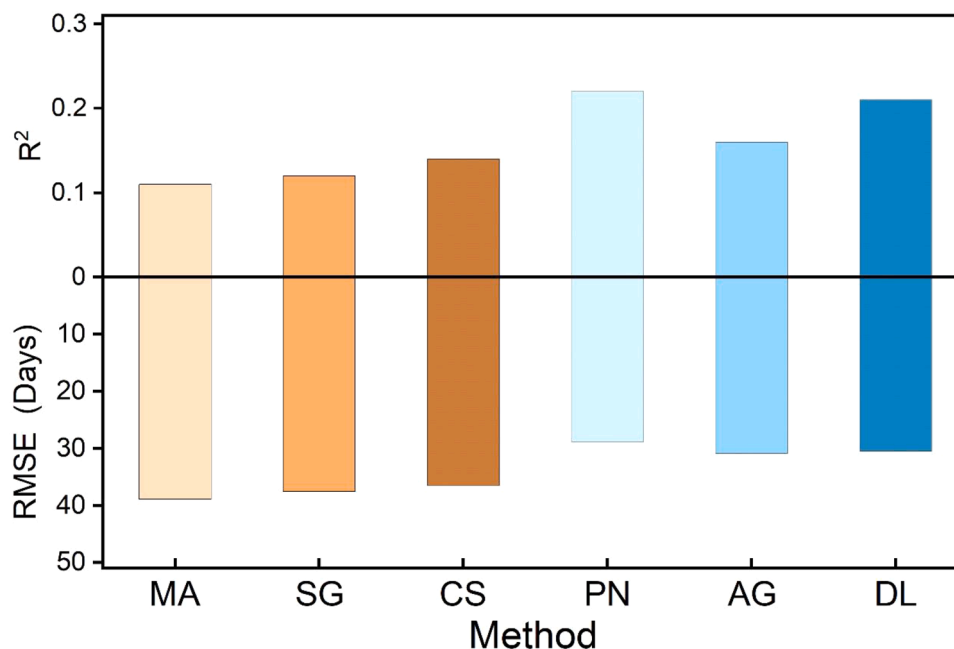

Fig. 9. Correlations between the peak photosynthesis timing (PPT) and the peak greenness timing (PGT). MA, SG, CS, PN, AG, and DL represent the moving averaging filter, Savitzky-Golay filter, cubic smoothing spline, polynomial, asymmetric Gaussian, and double logistic function, respectively.

PPT prediction for DBF, MF, and ENF. The principle of the fitting method and the physiological properties of the biome may result in performance differences. Lastly, we did not find an overall advancing PPT trend using GPP estimates from 48 flux sites. Our results suggest the principle of fitting methods and the physiological property of the biome are two main factors in PPT estimation. More importantly, PGT is not a good surrogate of PPT; therefore, the PPT trends on the regional scales based on VIs should be viewed with caution in previous studies.

Declaration of Competing Interest

Acknowledgments

Supplementary materials

Supplementary material associated with this article can be found, in the online version, at doi:10.1016/j.agrformet.2022.109054.

References

Atkinson, P.M., Jeganathan, C., Dash, J., Atzberger, C., 2012. Inter-comparison of four models for smoothing satellite sensor time-series data to estimate vegetation phenology. Remote Sens. Environ. 123, 400–417. https://doi.org/10.1016/j.rse.2012.04.001.

Bórnez, K., Richardson, A.D., Verger, A., Descals, A., Peñuelas, J., 2020. Evaluation of VEGETATION and PROBA-V phenology using phenocam and eddy covariance data. Remote Sens. (18), 12. https://doi.org/10.3390/RS12183077.

Cai, Z., Jönsson, P., Jin, H., Eklundh, L., 2017. Performance of smoothing methods for reconstructing NDVI time-series and estimating vegetation phenology from MODIS data. Remote Sens. 9 (12), 20–22. https://doi.org/10.3390/rs9121271.

Chang, Q., Xiao, X., Jiao, W., Wu, X., Doughty, R., Wang, J., Du, L., Zou, Z., Qin, Y., 2019. Assessing consistency of spring phenology of snow-covered forests as estimated by vegetation indices, gross primary production, and solar-induced chlorophyll fluorescence. Agric. For. Meteorol. 275 (May), 305–316. https://doi.org/10.1016/j.agrformet.2019.06.002.

Chen, J., Jönsson, P., Tamura, M., Gu, Z., Matsushita, B., Eklundh, L., 2004. A simple method for reconstructing a high-quality NDVI time-series data set based on the Savitzky-Golay filter. Remote Sens. Environ. 91 (3–4), 332–344. https://doi.org/10.1016/j.rse.2004.03.014.

Chen, J.M., Deng, F., Chen, M., 2006. Locally adjusted cubic-spline capping for reconstructing seasonal trajectories of a satellite-derived surface parameter. IEEE Trans. Geosci. Remote Sens. 44 (8), 2230–2237. https://doi.org/10.1109/TGRS.2006.872089.

Park, T., Chen, C., Macias-Fauria, M., Tømmervik, H., Choi, S., Winkler, A., Bhatt, U.S., Walker, D.A., Piao, S., Brovkin, V., Nemani, R.R., Myneni, R.B., 2019. Changes in timing of seasonal peak photosynthetic activity in northern ecosystems. Glob. Chang. Biol. 25 (7), 2382–2395. https://doi.org/10.1111/gcb.14638.

Cong, N., Piao, S., Chen, A., Wang, X., Lin, X., Chen, S., Han, S., Zhou, G., Zhang, X., 2012. Spring vegetation green-up date in China inferred from SPOT NDVI data: a multiple model analysis. Agric. For. Meteorol. 165, 104–113. https://doi.org/10.1016/j.agrformet.2012.06.009.

D'Odorico, P., Gonsamo, A., Gough, C.M., Bohrer, G., Morison, J., Wilkinson, M., Hanson, P.J., Gianelle, D., Fuentes, J.D., Buchmann, N., 2015. The match and mismatch between photosynthesis and land surface phenology of deciduous forests. Agric. For. Meteorol. 214–215, 25–38. https://doi.org/10.1016/j.agrformet.2015.07.005.

Elinav, E., Ben-Dov, I.Z., Ackerman, E., Kiderman, A., Glikberg, F., Shapira, Y., Ackerman, Z., 2005. Correlation between serum alanine aminotransferase activity and age: an inverted U curve pattern. Am. J. Gastroenterol. 100 (10), 2201–2204. https://doi.org/10.1111/j.1572-0241.2005.41822.x.

Elmore, A.J., Guinn, S.M., Minsley, B.J., Richardson, A.D., 2012. Landscape controls on the timing of spring, autumn, and growing season length in mid-Atlantic forests. Glob. Chang. Biol. 18 (2), 656–674. https://doi.org/10.1111/j.1365-2486.2011.02521.x.

Emmel, C., Winkler, A., Hörtnagl, L., Revill, A., Ammann, C., D'Odorico, P., Buchmann, N., Eugster, W., 2018. Integrated management of a Swiss cropland is not sufficient to preserve its soil carbon pool in the long term. Biogeosciences 15 (17), 5377–5393. https://doi.org/10.5194/bg-15-5377-2018.

Forkel, M., Migliavacca, M., Thonicke, K., Reichstein, M., Schaphoff, S., Weber, U., Carvalhais, N., 2015. Codominant water control on global interannual variability and trends in land surface phenology and greenness. Glob. Chang. Biol. 21 (9), 3414–3435. https://doi.org/10.1111/gcb.12950.

Gamon, J.A., Field, C.B., Goulden, M.L., Griffin, K.L., Hartley, A.E., Joel, G., Penuelas, J., Valentini, R., 1995. Relationships between NDVI, canopy structure, and photosynthesis in three Californian vegetation types. Ecol. Appl. 5 (1), 28–41. https://doi.org/10.2307/1942049.

Ge, Z., Huang, J., Wang, X., Zhao, Y., Tang, X., Zhou, Y., Lai, P., Hao, B., Ma, M., 2021. Using remote sensing to identify the peak of the growing season at globally-distributed flux sites: a comparison of models, sensors, and biomes. Agric. For. Meteorol. 307, 108489 https://doi.org/10.1016/j.agrformet.2021.108489.

Gonsamo, A., Chen, J.M., D'Odorico, P, 2013. Deriving land surface phenology indicators from CO2 eddy covariance measurements. Ecol. Indic. 29, 203–207. https://doi.org/10.1016/j.ecolind.2012.12.026.

Gonsamo, A., Chen, J.M., David, T.P., Kurz, W.A., Wu, C., 2012. Land surface phenology from optical satellite measurement and CO$_2$ eddy covariance technique. J. Geophys. Res. Biogeosci. 117 (3), 1–18. https://doi.org/10.1029/2012JG002070.

Gonsamo, A., Chen, J.M., Ooi, Y.W., 2018. Peak season plant activity shift towards spring is reflected by increasing carbon uptake by extratropical ecosystems. Glob. Chang. Biol. 24 (5), 2117–2128. https://doi.org/10.1111/gcb.14001.

Gonsamo, A., Chen, J.M., Wu, C., Dragoni, D., 2012. Predicting deciduous forest carbon uptake phenology by upscaling FLUXNET measurements using remote sensing data. Agric. For. Meteorol. 165, 127–135. https://doi.org/10.1016/j.agrformet.2012.06.006.

Gu, L., Baldocchi, D., Verma, S.B., Black, T.A., Vesala, T., Falge, E.M., Dowty, P.R., 2002. Advantages of diffuse radiation for terrestrial ecosystem productivity. J. Geophys. Res. Biogeosci. 107 (5–6) https://doi.org/10.1029/2001jd001242.

Gu, L., Post, W.M., Baldocchi, D.D., Black, T.A., Suyker, A.E., Verma, S.B., Vesala, T., Wofsy, S.C., 2009. Characterizing the seasonal dynamics of plant community photosynthesis across a range of vegetation types. Phenology of Ecosystem Processes: Applications in Global Change Research, 1st ed. Springer. https://doi.org/10.1007/978-1-4419-0026-5_2.

Guan, B.T., 2014. Ensemble empirical mode decomposition for analyzing phenological responses to warming. Agric. For. Meteorol. 194, 1–7. https://doi.org/10.1016/j.agrformet.2014.03.010.

Jones, M.O., Kimball, J.S., Jones, L.A., McDonald, K.C., 2012. Satellite passive microwave detection of North America start of season. Remote Sens. Environ. 123, 324–333. https://doi.org/10.1016/j.rse.2012.03.025.

Jönsson, P., Eklundh, L., 2002. Seasonality extraction by function fitting to time-series of satellite sensor data. IEEE Trans. Geosci. Remote Sens. 40 (8), 1824–1832. https://doi.org/10.1109/TGRS.2002.802519.

Jönsson, P., Eklundh, L., 2004. TIMESAT - a program for analyzing time-series of satellite sensor data. Comput. Geosci. 30 (8), 833–845. https://doi.org/10.1016/j.cageo.2004.05.006.

Klosterman, S.T., Hufkens, K., Gray, J.M., Melaas, E., Sonnentag, O., Lavine, I., Mitchell, L., Norman, R., Friedl, M.A., Richardson, A.D., 2014. Evaluating remote sensing of deciduous forest phenology at multiple spatial scales using PhenoCam imagery. Biogeosciences 11 (16), 4305–4320. https://doi.org/10.5194/bg-11-4305-2014.

Kong, D., Zhang, Y., Wang, D., Chen, J., Gu, X., 2020. Photoperiod explains the asynchronization between vegetation carbon phenology and vegetation greenness phenology. J. Geophys. Res. Biogeosci. 125 (8), 1–15. https://doi.org/10.1029/2020JG005636.

Li, J., Wu, C., Wang, X., Peng, J., Dong, D., Lin, G., 2020. Satellite observed indicators of the maximum plant growth potential and their responses to drought over Tibetan Plateau (1982 –2015). Ecol. Indic. 108 (September 2019), 105732 https://doi.org/10.1016/j.ecolind.2019.105732.

Li, Xing, Xiao, J., He, B., Altaf Arain, M., Beringer, J., Desai, A.R., Emmel, C., Hollinger, D.Y., Krasnova, A., Mammarella, I., Noe, S.M., Ortiz, P.S., Rey-Sanchez, A.C., Rocha, A.V., Varlagin, A, 2018. Solar-induced chlorophyll fluorescence is strongly correlated with terrestrial photosynthesis for a wide variety of biomes: first global analysis based on OCO-2 and flux tower observations. Glob. Chang. Biol. 24 (9), 3990–4008. https://doi.org/10.1111/gcb.14297.

Li, Xuecao, Zhou, Y., Asrar, G.R., Mao, J., Li, X., Li, W., 2017. Response of vegetation phenology to urbanization in the conterminous United States. Glob. Chang. Biol. 23 (7), 2818–2830. https://doi.org/10.1111/gcb.13562.

Migliavacca, M., Galvagno, M., Cremonese, E., Rossini, M., Meroni, M., Sonnentag, O., Cogliati, S., Manca, G., Diotri, F., Busetto, L., Cescatti, A., Colombo, R., Fava, F., Morra di Cella, U., Pari, E., Siniscalco, C., Richardson, A.D., 2011. Using digital repeat photography and eddy covariance data to model grassland phenology and photosynthetic CO$_2$ uptake. Agric. For. Meteorol. 151 (10), 1325–1337. https://doi.org/10.1016/j.agrformet.2011.05.012.

Muraoka, H., Koizumi, H., 2005. Photosynthetic and structural characteristics of canopy and shrub trees in a cool-temperate deciduous broadleaved forest : implication to the ecosystem carbon gain. Agric. For. Meteorol. 134, 39–59. https://doi.org/10.1016/j.agrformet.2005.08.013.

Park, T., Chen, C., Macias, M., Tømmervik, H., Choi, S., Winkler, A., Bhatt, U.S., Walker, D.A., Piao, S., Brovkin, V., Nemani, R.R., Myneni, R.B., 2019. *Changes in timing of seasonal peak photosynthetic activity in northern ecosystems. March*, pp. 2382–2395. https://doi.org/10.1111/gcb.14638.

Paruelo, J.M., Jobbágy, E.G., Sala, O.E., 2001. Current distribution of ecosystem functional types in temperate South America. Ecosystems 4 (7), 683–698. https://doi.org/10.1007/s10021-001-0037-9.

Pastorello, G., Trotta, C., Canfora, E., Chu, H., Christianson, D., Cheah, Y.W., Poindexter, C., Chen, J., Elbashandy, A., Humphrey, M., Isaac, P., Polidori, D., Ribeca, A., van Ingen, C., Zhang, L., Amiro, B., Ammann, C., Arain, M.A., Ardö, J., Papale, D., 2020. The FLUXNET2015 dataset and the ONEFlux processing pipeline for eddy covariance data. Scientific Data 7 (1), 225. https://doi.org/10.1038/s41597-020-0534-3.

Piao, S., Fang, J., Zhou, L., Ciais, P., Zhu, B., 2006. Variations in satellite-derived phenology in China's temperate vegetation. Glob. Chang. Biol. 12 (4), 672–685. https://doi.org/10.1111/j.1365-2486.2006.01123.x.

Richardson, A.D., Hufkens, K., Milliman, T., Aubrecht, D.M., Chen, M., Gray, J.M., Johnston, M.R., Keenan, T.F., Klosterman, S.T., Kosmala, M., Melaas, E.K., Friedl, M. A., Frolking, S., 2018. Tracking vegetation phenology across diverse North American biomes using PhenoCam imagery. Sci. Data 5, 1–24. https://doi.org/10.1038/sdata.2018.28.

Rodrigues, A., Marcal, A.R.S., Cunha, M., 2012. Phenology parameter extraction from time-series of satellite vegetation index data using phenosat. In: International Geoscience and Remote Sensing Symposium (IGARSS), pp. 4926–4929. https://doi.org/10.1109/IGARSS.2012.6352507.

Schubert, P., Lund, M., Ström, L., Eklundh, L., 2010. Impact of nutrients on peatland GPP estimations using MODIS time series data. Remote Sens. Environ. 114 (10), 2137–2145. https://doi.org/10.1016/j.rse.2010.04.018.

Shen, M., Tang, Y., Desai, A.R., Gough, C., Chen, J., 2014. Can EVI-derived land-surface phenology be used as a surrogate for phenology of canopy photosynthesis? Int. J. Remote Sens. 35 (3), 1162–1174. https://doi.org/10.1080/01431161.2013.875636.

Tang, G., Arnone, J.A., Verburg, P.S.J., Jasoni, R.L., Sun, L., 2015. Trends and climatic sensitivities of vegetation phenology in semiarid and arid ecosystems in the US Great Basin during 1982-2011. Biogeosciences 12 (23), 6985–6997. https://doi.org/10.5194/bg-12-6985-2015.

Testa, S., Soudani, K., Boschetti, L., Borgogno Mondino, E., 2018. MODIS-derived EVI, NDVI and WDRVI time series to estimate phenological metrics in French deciduous forests. Int. J. Appl. Earth Obs. Geoinf. 64 (August 2017), 132–144. https://doi.org/10.1016/j.jag.2017.08.006.

Tian, J., Zhu, X., Chen, J., Wang, C., Shen, M., Yang, W., Tan, X., Xu, S., Li, Z., 2021. Improving the accuracy of spring phenology detection by optimally smoothing satellite vegetation index time series based on local cloud frequency. ISPRS J. Photogramm. Remote Sens. 180 (August), 29–44. https://doi.org/10.1016/j.isprsjprs.2021.08.003.

Wang, H., Chen, J., Wu, Z., Lin, H., 2012. Rice heading date retrieval based on multi-temporal MODIS data and polynomial fitting. Int. J. Remote Sens. 33 (6), 1905–1916. https://doi.org/10.1080/01431161.2011.603378.

Wang, R., Chen, J.M., Liu, Z., Arain, A., 2017. Evaluation of seasonal variations of remotely sensed leaf area index over five evergreen coniferous forests. ISPRS J. Photogramm. Remote Sens. 130 (2012), 187–201. https://doi.org/10.1016/j.isprsjprs.2017.05.017.

Wang, Xian, Dannenberg, M.P., Yan, D., Jones, M.O., Kimball, J.S., Moore, D.J.P., van Leeuwen, W.J.D., Didan, K., Smith, W.K., 2020. Globally consistent patterns of asynchrony in vegetation phenology derived from optical, microwave, and fluorescence satellite data. J. Geophys. Res. Biogeosci. 125 (7), 0–3. https://doi.org/10.1029/2020JG005732.

Wang, Xiaoyue, Wu, C., 2019. Estimating the peak of growing season (POS) of China's terrestrial ecosystems. Agric. For. Meteorol. 278, 107639 https://doi.org/10.1016/j.agrformet.2019.107639.

Wang, Xiaoyue, Wu, C., Peng, D., Gonsamo, A., Liu, Z., 2018. Snow cover phenology affects alpine vegetation growth dynamics on the Tibetan Plateau: satellite observed evidence, impacts of different biomes, and climate drivers. Agric. For. Meteorol. 256–257 (May 2017), 61–74. https://doi.org/10.1016/j.agrformet.2018.03.004.

Wang, Xufeng, Xiao, J., Li, X., Cheng, G., Ma, M., Che, T., Dai, L., Wang, S., Wu, J, 2017. No consistent evidence for advancing or delaying trends in spring phenology on the Tibetan plateau. J. Geophys. Res. Biogeoscien. 122 (12), 3288–3305. https://doi.org/10.1002/2017JG003949.

Wang, Xufeng, Xiao, J., Li, X., Cheng, G., Ma, M., Zhu, G., Altaf Arain, M., Andrew Black, T., Jassal, R.S, 2019. No trends in spring and autumn phenology during the global warming hiatus. Nat. Commun. 10 (1), 1–10. https://doi.org/10.1038/s41467-019-10235-8.

Wu, C., Chen, J.M., Black, T.A., Price, D.T., Kurz, W.A., Desai, A.R., Gonsamo, A., Jassal, R.S., Gough, C.M., Bohrer, G., Dragoni, D., Herbst, M., Gielen, B.,

Berninger, F., Vesala, T., Mammarella, I., Pilegaard, K., Blanken, P.D., 2013. Interannual variability of net ecosystem productivity in forests is explained by carbon flux phenology in autumn. Glob. Ecol. Biogeogr. 22 (8), 994–1006. https://doi.org/10.1111/geb.12044.

Wu, C., Gonsamo, A., Chen, J.M., Kurz, W.A., Price, D.T., Lafleur, P.M., Jassal, R.S., Dragoni, D., Bohrer, G., Gough, C.M., Verma, S.B., Suyker, A.E., Munger, J.W., 2012. Interannual and spatial impacts of phenological transitions, growing season length, and spring and autumn temperatures on carbon sequestration: a North America flux data synthesis. Glob. Planet. Chang. 92–93, 179–190. https://doi.org/10.1016/j.gloplacha.2012.05.021.

Wu, C., Peng, D., Soudani, K., Siebicke, L., Gough, C.M., Arain, M.A., Bohrer, G., Lafleur, P.M., Peichl, M., Gonsamo, A., Xu, S., Fang, B., Ge, Q., 2017. Land surface phenology derived from normalized difference vegetation index (NDVI) at global FLUXNET sites. Agric. For. Meteorol. 233, 171–182. https://doi.org/10.1016/j.agrformet.2016.11.193.

Wu, X., Babst, F., Ciais, P., Frank, D., Reichstein, M., Wattenbach, M., Zang, C., Mahecha, M.D., 2014. Climate-mediated spatiotemporal variability in terrestrial productivity across Europe. Biogeosciences 11 (11), 3057–3068. https://doi.org/10.5194/bg-11-3057-2014.

Xiao, J., Fisher, J.B., Hashimoto, H., Ichii, K., Parazoo, N.C., 2021. Emerging satellite observations for diurnal cycling of ecosystem processes Jingfeng. Nat. Plants 7 (7), 877–887. https://doi.org/10.1038/s41477-021-00952-8.

Xiao, X., Hagen, S., Zhang, Q., Keller, M., Moore, B., 2006. Detecting leaf phenology of seasonally moist tropical forests in South America with multi-temporal MODIS images. Remote Sens. Environ. 103 (4), 465–473. https://doi.org/10.1016/j.rse.2006.04.013.

Xu, C., Liu, H., Williams, A.P., Yin, Y., Wu, X., 2016. Trends toward an earlier peak of the growing season in Northern Hemisphere mid-latitudes. Glob. Chang. Biol. 22 (8), 2852–2860. https://doi.org/10.1111/gcb.13224.

Xu, H., Xiao, J., Zhang, Z., 2020. Heatwave effects on gross primary production of northern mid-latitude ecosystems. Environ. Res. Lett. (7), 15. https://doi.org/10.1088/1748-9326/ab8760.

Xu, X., Du, H., Fan, W., Hu, J., Mao, F., Dong, H., 2019. Long-term trend in vegetation gross primary production, phenology and their relationships inferred from the FLUXNET data. J. Environ. Manag. 246 (January), 605–616. https://doi.org/10.1016/j.jenvman.2019.06.023.

Yang, J., Dong, J., Xiao, X., Dai, J., Wu, C., Xia, J., Zhao, G., Zhao, M., Li, Z., Zhang, Y., Ge, Q., 2019. Divergent shifts in peak photosynthesis timing of temperate and alpine grasslands in China. Remote Sens. Environ. 233 (August), 111395 https://doi.org/10.1016/j.rse.2019.111395.

Yang, L., Noormets, A., 2021. Standardized flux seasonality metrics: a companion dataset for FLUXNET annual producta. Earth Syst. Sci. Data 13 (4), 1461–1475. https://doi.org/10.5194/essd-13-1461-2021.

Yin, G., Verger, A., Filella, I., Descals, A., Peñuelas, J., 2020. Divergent estimates of forest photosynthetic phenology using structural and physiological vegetation indices. Geophys. Res. Lett. 47 (18), e2020GL089167 https://doi.org/10.1029/2020GL089167.

Yuan, H., Wu, C., Lu, L., Wang, X., 2018. A new algorithm predicting the end of growth at five evergreen conifer forests based on nighttime temperature and the enhanced vegetation index. ISPRS J. Photogram. Remote Sens. 144 (May), 390–399. https://doi.org/10.1016/j.isprsjprs.2018.08.013.

Zhang, X., Friedl, M.A., Schaaf, C.B., Strahler, A.H., Liu, Z., 2005. Monitoring the response of vegetation phenology to precipitation in Africa by coupling MODIS and TRMM instruments. J. Geophys. Res. D Atmos. 110 (12), 1–14. https://doi.org/10.1029/2004JD005263.

Zhao, B., Donnelly, A., Schwartz, M.D., 2020. Evaluating autumn phenology derived from field observations, satellite data, and carbon flux measurements in a northern mixed forest, USA. Int. J. Biometeorol. 64 (5), 713–727. https://doi.org/10.1007/s00484-020-01861-9.

Zhou, Y., Wu, X., Ju, W., Chen, J.M., Wang, S., Wang, H., Yuan, W., Andrew Black, T., Jassal, R., Ibrom, A., Han, S., Yan, J., Margolis, H., Roupsard, O., Li, Y., Zhao, F., Kiely, G., Starr, G., Pavelka, M., Varlagin, A., 2016. Global parameterization and validation of a two-leaf light use efficiency model for predicting gross primary production across FLUXNET sites. J. Geophys. Res. G: Biogeoscis. 121 (4), 1045–1072. https://doi.org/10.1002/2014JG002876.